Combustion and Flame 240 (2022) 112008

Contents lists available at ScienceDirect

Combustion and Flame

journal homepage: www.elsevier.com/locate/combustflame

Horizontal flame spread over thin solids in reduced buoyancy environments

Chuanjia Wu [a,b,1], Yuan Xiao [c,1], Shuangfeng Wang [a,b,d,*], Feng Zhu [a]

[a] Key Laboratory of Microgravity, Institute of Mechanics, Chinese Academy of Sciences, Beijing 100190, China
[b] School of Engineering Science, University of Chinese Academy of Sciences, Beijing 100049, China
[c] School of Mechatronics & Vehicle Engineering, East China Jiaotong University, Nanchang 330013, Jiangxi, China
[d] State Key Laboratory of High-Temperature Gas Dynamics, Chinese Academy of Sciences, Beijing 100190, China

ARTICLE INFO

Article history:
Received 28 June 2021
Revised 17 January 2022
Accepted 19 January 2022
Available online 31 January 2022

Keywords:
Flame spread
Buoyancy
Partial gravity
Horizontal channel
Thermoconvective instabilities

ABSTRACT

A Horizontal Channel Apparatus (HCA) has been employed to investigate opposed flame spread over solid fuels in reduced buoyancy environments, which would be encountered at the diminished gravitational levels on extraterrestrial surfaces (e.g., the partial gravity on the Moon and Mars) as well. With a scaling analysis, the characteristic buoyant flow velocity in HCA is well correlated to the channel height and the Rayleigh (*Ra*) number. The experimental results show that, without forced flow, the flame spread rate and flammability in HCA can be correlated with those at different gravity levels by using *Ra* number, indicating HCA may have the ability to simulate the burning characters in partial gravity. Together with the Reynolds (*Re*) and *Ra* numbers, which signify the role of forced and buoyant flow, respectively, the flame spread rates and the map of flammability of the solid fuel obtained in the current HCA experiments are determined. Furthermore, four distinctively different flame spread patterns are found at various channel heights and opposed-flow velocities once the width of the cellulosic sample is extended. Likewise, the map of flame spread patterns is governed by the *Re* and *Ra*. It is further found through the examinations of the time average of the mass-loss rate that as long as *Ra* is below a critical value, the opposed flow in terms of *Re* mainly determines the oxygen transportation, while the reduced buoyancy in terms of *Ra* mainly contributes to the bifurcations of the potential hydro/thermal instabilities.

1. Introduction

Flame spread over solid combustibles is inherently a reacting boundary flow with low speed [1], in which the hydro and thermal dynamics determine its global characteristic, e.g. flame spread rate and flammability boundary. The bulk ambient flow involved in the flame spread could be either buoyancy-driven convection, mechanically driven advection, or mixing convection of both. Specially, as it is always fully developed in the open terrestrial environment, the buoyancy-induced flow determines the heat and mass transfer as studied previously [2–7]. Nevertheless, in the microgravity (Mg) environment, the almost eliminations of the buoyancy-driven flow enable the observations of flame spread near the quenching limit, in which the distinctively different burning characteristics are revealed [8–11].

In addition to the microgravity environment, the buoyancy-driven flow can also be significantly suppressed in confined geometry, once the corresponding Rayleigh number (*Ra*) is below the critical value. The horizontal narrow channel apparatus (NCA) is designed based on this principle. Ivanov et al. [12] used NCA to investigate the flame spread over nonmetallic-material and found that the flame spread rates of different materials measured from the NCA correlate well with those obtained from Mg experiments. Olson et al. [13] used the same apparatus to investigate the solid fuel burning behaviors and their experimental results showed that 10-mm height NCA can capture the essential features of flame spread in the microgravity, indicating the NCA can functionally simulate microgravity conditions. Zik et al. [14–16] proposed the NCA to suppress the buoyancy induced by the smoldering combustion. They successfully observed the same “fingering” instability pattern as those observed in microgravity experiments in space [13,17]. The size of each “finger”, as well as their in-between gaps, are excellently correlated with the Péclet number. Zhang et al. [18] found that once half of the sample width is larger than the oxygen diffusion length, the flame will break into flamelets due to

* Corresponding author at: 15 Bei-Si-Huan-Xi Road, Institute of Mechanics, Chinese Academy of Sciences, Beijing 100190, China.
E-mail address: sfwang@imech.ac.cn (S. Wang).
[1] Both the authors contributed equally to this work.

https://doi.org/10.1016/j.combustflame.2022.112008
0010-2180/

the oxygen shortage. Wang et al. [19] investigated the quenching limit instabilities of concurrent flame spread by employing the NCA. Two kinds of instabilities are identified, namely finger instability and traveling wave instability. The oxygen concentration determines which kind of instability prevails the flame spread. Among a variety of investigations with NCA on influences of thermally thin/thick material [19–25], the heat loss [26], and fire suppressants [27] have been thoroughly examined.

The above studies mainly focus on the flame spread behavior in which the buoyancy-driven flow is almost eliminated. However, when the buoyancy-driven flow is not thoroughly but "partly" suppressed, the flame spread may behave quite differently. Such buoyancy-reduced environments would be encountered at the diminished gravitational levels on extraterrestrial surfaces (e.g., the partial gravity on the Moon and Mars). To investigate the burning characteristics at partial gravity conditions, Sacksteder and T'ien [28] (abbreviated as SA94 hereafter) conducted downward flame spread in a parabolic-trajectory airplane. It was found that the flame spread rates show the non-monotonic variation with the increased gravity and the lowest oxygen concentration to sustain the flame spread is at 14%, lower than that recorded in the Mg and terrestrial experiments [8,10]. This experiment indicates that there could be a higher fire risk in the buoyancy-reduced environment.

The channel with a height of 10 mm is often used to investigate the burning characters in buoyancy-suppressed environments. However, the buoyancy level will be increased with the channel height. That means if a horizontal geometry whose characteristic size is neither "narrow" nor sufficiently "large", the flame spread within may be similar to those at partial gravity conditions. To distinguish from the NCA, such horizontal geometry with expanded vertical length scale is proposed as the "Horizontal Channel Apparatus" (HCA) by this study.

Once the buoyancy-driven flow is enhanced in the HCA compared to those in the NCA, more complicated hydro and thermal dynamics are involved. For instance, if there is forced flow in the horizontal channel, the flame spread in the HCA is determined by the strong coupling between the buoyancy-driven flow, and the horizontally advective boundary layer flow, e.g. the Oseen flow assumed by deRis [29] and other boundary flow such as [2,30] studied. In addition, even regardless of the flame spread dynamics, such complex thermal-advective boundary layer flow involve different flow instability as well as their transitions to each other. For instance, the Rayleigh-Benard-Poiseuille (RBP) flow occurs in a similar horizontal geometry as the HCA, in which the thermally convective flow driven by heated bottom plate concur with the forced advective flow with Poiseuille velocity profile. It was well known for the hydro/thermal dynamic community that for the RBP flow, the flow structures/pattern would transfer from the longitude rolls whose axis is parallel with the flow direction to the transverse rolls whose axis is orthogonal to the flow and temperature gradient direction, under the competitions between the convective and advective flow, namely, Rayleigh number and Reynolds (Re) number [31]. Analogously, if the channel height of the NCA is increased so that the convective flow induced by flame is no longer negligible, the enhanced competition between the convective and advective flow may also incite distinctively different flame spread pattern from the "fingering" instability near the quenching limit may arise as well. The potential different flame spread patterns within HCA will be reported later by this study.

To investigate flame spread behaviors in reduced buoyancy environments, this study designs a HCA with the channel height ranging from 5 mm which is lower than the typical 10 mm height NCA [13,18,20,25,26,32,33] to 100 mm where the flame geometry is far away from the channel wall. Such a range of channel height allows this paper to extend the buoyancy in terms of Ra from the order of 10^3 where the diffusive flame spread near the quenching limit exists to the order of $10^7 \sim 10^8$ where the typical flame spread on terrestrial environments occurs [34,35]. Correspondingly, a "reduced buoyancy environment" for the flame spread refers to where the buoyancy induced by the flame varies within such Ra spectrum.

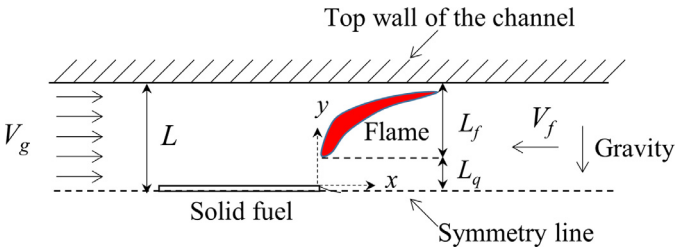

Fig. 1. Schematic of the opposed flame spread in the HCA.

This paper is organized as follows. The scaling analysis, which aims to correlate the buoyancy-driven velocity in the partial gravity environment and the HCA, is presented in §2, followed by the experimental procedures described in §3. The global characteristics (the stable flame spread rates and the map of flammability) of the flame spread over narrow samples in the HCA are reported in §4.1 and §4.2. §4.3 demonstrates the different flame spread patterns behaviors as well as the map of their effective regions in terms of the channel height and opposed flow velocity, alternatively, Ra and Re. At last, the conclusions are made in §5.

2. Scaling analysis: the dependence of buoyancy on channel height

Two parameters are proposed to characterize the buoyancy level in the HCA. The first is the characteristic buoyant flow velocity V_b, which is derived from the momentum balance during the stable flame spread. The second is the Rayleigh number Ra, a traditional yet universal governing parameter to describe the phenomena related to thermal convection. For the flame spread, Ra is defined as:

$$Ra = \frac{g(T_f - T_\infty)L_c^3}{T_\infty \nu \alpha_g} \tag{1}$$

where L_c represents the characteristic length scale. For the flame spread in the HCA, $L_c = L$ is appropriate based on the traditional definitions used in the hydro/thermal dynamic community. For the flame spread in partial gravity environments, L_c is estimated by V_b as will be shown later. As both V_b and Ra could associate the local gravitational acceleration g with the channel height of the HCA, based on V_b and Ra it is likely to correlate the global characteristics of the flame spread in partial gravity environment and the HCA.

Figure 1 schematically delineates the opposed flame spread over solid fuels involving several characteristic length scales, that is, L_f represents the flame height and L_q represents standoff distance or quenching distance. Assuming the heat conduction from the gas to solid phase predominately results in the preheat of the solid fuel, the length scale in the solid phase L_s is estimated as [36–38]:

$$L_s \sim \frac{\alpha_s}{V_f} \tag{2}$$

where α_s is the thermal diffusivity of the solid fuel and V_f is the flame spread rate. Assuming the energy balance between gaseous heat conduction and convection results in the preheat zone of the gas phase, L_g is estimated as [36–38]:

$$L_g \sim \frac{\alpha_g}{V_g + V_f} \tag{3}$$

where α_g and V_g are the thermal diffusivity and the opposed flow velocity of the gaseous mixture, respectively. In the environment without forced flow, only buoyancy-driven flow is produced, therefore $V_g = V_b$, where V_b is the characteristic velocity of the buoyancy-driven flow. Based on experimental results, V_b is usually one order larger than V_f in purely buoyancy-induced opposed flame spread, V_f could be neglected [39]. As a result, $L_{g,b}$, which indicates L_g only associated with the buoyancy, is estimated as:

$$L_{g,b} \sim \frac{\alpha_g}{V_b} \tag{4}$$

For the vertically opposed flame spread in the buoyant flow, the momentum balance in the vertical direction satisfies:

$$\rho_g V_b^2 \sim \rho_g \beta g (T_f - T_\infty) L_{g,b} \sim \rho_g \beta g (T_f - T_\infty) \frac{\alpha_g}{V_b} \tag{5}$$

where ρ_g represents the density of the gas phase, β represents the coefficient of volumetric expansion, T_f and T_∞ represent the flame and ambient temperature, respectively. Thus, an estimation of V_b is:

$$V_b \sim \left[\alpha_g \beta g (T_f - T_\infty)\right]^{1/3} \tag{6}$$

which agree with the estimations of V_b in [8,28,36,39,40].

For the opposed flame spread in the HCA, the limited channel height not only suppresses the buoyancy-driven flow but also subdues the development of the flame itself via geometrical suppression and heat loss to the channel wall [18,26,41–43]. If the channel height L is less than L_q, there is no space for gaseous reaction and therefore flame spread is no longer sustained. Such extinction is a result of spatial suppression when $L < L_q$ corresponds to the "quenching limit" of the opposed flame spread as reported in previous studies on the flame spread with the NCA [13,18,24,44]. If L is sufficiently large so that the geometrical suppression of the flame no longer exists, V_b within the HCA is almost as same as those in the open space. That is to say, the buoyancy-driven flow is fully developed, therefore the corresponding opposed flame spread in the HCA behaves equivalently as those in the open space. Based on the fully developed buoyancy-driven flow, an upper channel height L_{open} satisfies when $L > L_{open}$, $V_{b,HCA} = V_{b,open}$ where the subscripts "HCA" and "open" represent the HCA and open environment, respectively. For the channel height satisfying $L_q < L < L_{open}$, the flame geometry is more or less confined. Particularly, the heat loss from the flame to the channel wall would further reduce the effective flame height in the HCA, that is, $L_f < L - L_q$. On the contrary, there is always ample space for the pyrolysis of the solid fuel, that is to say, L_q remains the same in the HCA compared to that in the open environment. Consequently, it is proposed in this paper that the effective length scale $L_{b,HCA}$ in which the buoyancy-driven flow is developing satisfies:

$$L_{b,HCA} \sim L - L_q \sim L - \frac{\alpha_g}{V_f} \tag{7}$$

replacing L_g in Eq. (5) with $L_{b,HCA}$ yields:

$$\rho_g V_{b,HCA}^2 \sim \rho_g \beta g (T_f - T_\infty)(L - L_q) \sim \rho_g \beta g (T_f - T_\infty)\left(L - \frac{\alpha_g}{V_f}\right) \tag{8}$$

where $V_{b,HCA}$ represents V_b in the HCA. Therefore, $V_{b,HCA}$ is estimated as:

$$V_{b,HCA} \sim \left[\beta g (T_f - T_\infty)\left(L - \frac{\alpha_g}{V_f}\right)\right]^{1/2} \tag{9}$$

unlike V_b in Eq. (6), $V_{b,HCA}$ is associated with measured V_f. Together with Eqs. (6) and (9), the velocity of the buoyancy-driven flow in the open environment and the confined HCA could be correlated with V_b:

$$V_b \sim \left[\alpha_g \beta g (T_f - T_\infty)\right]^{1/3} \sim \left[\beta g (T_f - T_\infty)\left(L - \frac{\alpha_g}{V_f}\right)\right]^{1/2} \tag{10}$$

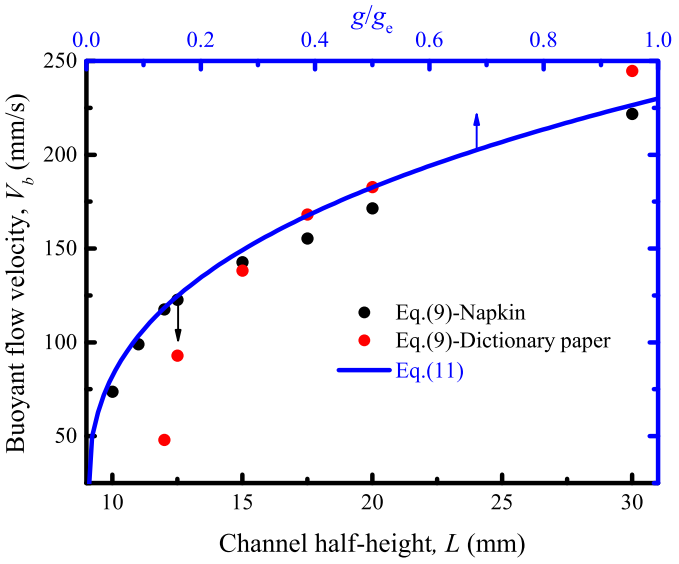

Fig. 2. The correlation of V_b between Eq. (11) and experimental data from the HCA. The solid line denotes Eq. (11) and the scattered points refer to the measurements of $V_{b,HCA}$ based on Eq. (9).

With Eq. (10), the correlations between $V_{b,HCA}$ in the current HCA, and V_b in the SA94 could be obtained. The property values for calculations are listed in Table 1. Based on Eq. (10), $V_{b,HCA}$ in the HCA require individual measurements of V_f, which inherently include the influences of the solid phase length scale L_s. Therefore only scattered points are obtained for $V_{b,HCA}$.

To test the effectiveness of Eq. (10), two thermally thin fuels, napkin and dictionary paper are selected. The area density of the napkin is very similar to those reported in SA 94, while the area density of the dictionary paper is 14 g/m^2 larger than that of the napkin paper. By setting an undermined constant c_{BC} in the following form:

$$V_b = c_{BC}\left[\alpha_g \beta g (T_f - T_\infty)\right]^{1/3} = V_{b,HCA} = \left[\beta g (T_f - T_\infty)\left(L - \frac{\alpha_g}{V_f}\right)\right]^{1/2} \tag{11}$$

the correlated results are shown in Fig. 2. Good correlation is obtained for the napkin paper whose area density is very close to the one reported in SA94, while deviations occur for the dictionary paper whose area density is larger, especially for the range of NCA where L = 12 and 14 mm. Such deviations are attributed to the inherent incompatibility between g/g_e and L in the partial gravity environment and buoyancy-suppressed environment. To solve this issue, further modifications are needed.

To harmonize the role of g/g_e and L, in describing the buoyancy, the non-dimensional quantity Ra is proposed. For the HCA, the characteristic length scale L_c to define Ra is appropriately selected as the channel height, inheriting the convection from the heat transfer community. As none of the characteristic length scales mentioned in Fig. 1 are clearly reported by SA94, the corresponding L_c, as well as Ra, need to be indirectly estimated. When the opposed flame spread is stable, the different length scales related are always geometrically similar, so that $L_c \sim L_g$. Based on Eqs. (4) and (6), L_c is related to V_b as:

$$L_c \sim L_g \sim \frac{\alpha_g}{V_b} \sim \frac{\alpha_g}{\left[\alpha_g \beta g (T_f - T_\infty)\right]^{1/3}} \tag{12}$$

accordingly, Ra corresponding to the experimental results from SA94 could be estimated based on L_c. Together with Ra directly obtained by channel height L of the HCA, the flame spread within

Table 1
Parameter values for calculations. The values corresponding to the gas phase are chosen at the vaporization temperature T_v = 618 K.

Properties	Symbols	Values	Units	References
Area density	ρ_{area}	8.5	g/m^2	–
Thermal diffusivity of gas phase	α_g	8.06 × 10^{-5}	m^2/s	[45]
Emissivity	ε	0.85	–	–
Thermal conductivity of gas phase	λ_g	4.79 × 10^{-2}	W/m/K	[45]
Stefan–Boltzmann constant	σ	5.67 × 10^{-8}	W/m^2/K^4	–
Viscosity	ν	5.54 × 10^{-5}	m^2/s	[45]
Heat capacity of solid phase	c_s	1063	J/kg/K	[5]
Gravitational acceleration on earth	g_e	9.81	m/s^2	–
Flame temperature	T_f	1500	K	[46]
Vaporization temperature	T_v	618	K	[5]
Ambient temperature	T_∞	300	K	–

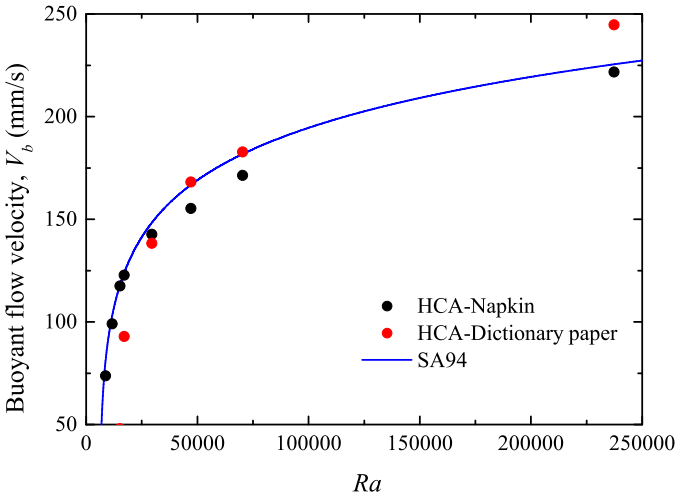

Fig. 3. The correlation of V_b with *Ra*. The solid line denotes V_b in SA94 and the scattered points refer to the measurements of $V_{b,HCA}$.

HCA could be correlated with those from SA94, as shown in Fig. 3.

Compare to Figure 2, the *Ra* correlation significantly improves the incompatibility issue of the dictionary paper. This is because the discrepancies for different thermally thin fuels are inherently included in the characteristic length scale $L_c \sim \alpha_g/V_b \sim \alpha_g/[\beta g(T_f - T_\infty)(L - \alpha_g/V_f)]^{1/2}$ inside the definition of *Ra*. A slight deviation is still found when $Ra < 25{,}000$ ($L < 15$ mm), which is perhaps ascribed to the enhanced role of radiations that are not considered in the current scaling analysis. Nevertheless, such *Ra* range is below the "buoyancy-reduced" environment and is more close to the "buoyancy-suppressed" environment such as NCA. Hence, based on Fig. 3, the *Ra* correlation is sufficient to capture the essential flame spread behaviors at the buoyancy-reduced environment. The effectiveness of *Ra* correlation will be constantly demonstrated in the following context, along with the other effective dimensionless governing parameter *Re* in a mixed convection environment.

3. Experiments

As schematically shown in Fig. 4, the HCA employed in this study consists of a rectangular horizontal channel and an inlet flow supply section. The ambient atmosphere of the O_2/N_2 mixture is achieved via two mass flow controllers (Alicat Scientific, type MC), which separately specify the mass flow rate of the pure oxygen and nitrogen flow. After sufficient mixing of pure oxygen and nitrogen flow within an ample mixing chamber, the O_2/N_2 mixture flow through an alumina chamber, in which a honeycomb gas diffuser and a contracting section are set up to ensure the uniformity of the oxidizer flow before it enters the HCA test section. The test section is a rectangular quartz channel with lateral sides sealed. The length and width of the channel are 900 mm and 360 mm. The distance between the sample and the contracting section is about 500 mm which is long enough to have a fully developed flow. The height of the HCA channel is adjustable in the range of 5 ∼ 100 mm so that a two-dimensional flow is obtained as the channel width is more than 3.6 times its maximum height.

The solid fuels for tests are napkins whose area density is 8.5 g/m^2 as listed in Table 1. For each test, the sample fuels are tapped to and sufficiently stretched by the frame of the stainless steel sample holder, which assures the effective area of the fixed sample fuel. The narrower samples with 35 mm width and the wider samples with 200 mm are used in the experiments. The lengths of the test fuels are all 255 mm. The igniter, which is a resistance of 4 ohms under 24 V as the igniter is switched, is placed at the downstream end of the sample holder to provide uniform ignition on the test fuels.

The experimental procedures for each test are as follows. For preparations, the fixed and stretched sample fuel on the sample holder was well adjusted, so that the test sample was horizontally symmetric to the central line of the channel and in the middle plane of the top and bottom plates of the HCA. Once the O_2/N_2 mixture gas flow with desired mass fractions for oxygen and nitrogen is initialized and fully developed within the test channel, the igniter was switched on. Only for the purely buoyant flow environment tests, after the full development of the O_2/N_2 mixture flow, the gas supply was shut off and the outlet of the channel was immediately sealed for several minutes to ensure the establishment of the desired ambient before the ignition. The igniter was turned off as long as the flame was completely spread away. The entire ignition and flame spread process were recorded by two digital video cameras (Sony DCR-TRV 900E and Nikon D7200, with a frame rate of 25 fps) at both top and side of the HCA.

All cases include three to five repeated tests to guarantee reliability and obtain an average value. Based on the analysis of flame images, the flame spread rates are calculated according to the spread track in the center of the overall flame/flamelet edge. The relative errors of oxygen concentration, channel heights, and sample area densities are estimated at ±1%, ±1%, and ±5%. The precision of flow controller precision is ±1%, providing a precision of ±2% for the gas flow velocities in the forced flow experiments. Depending on the ambiguity of the flame position, the measurement error of the flame spread rate is ±5%.

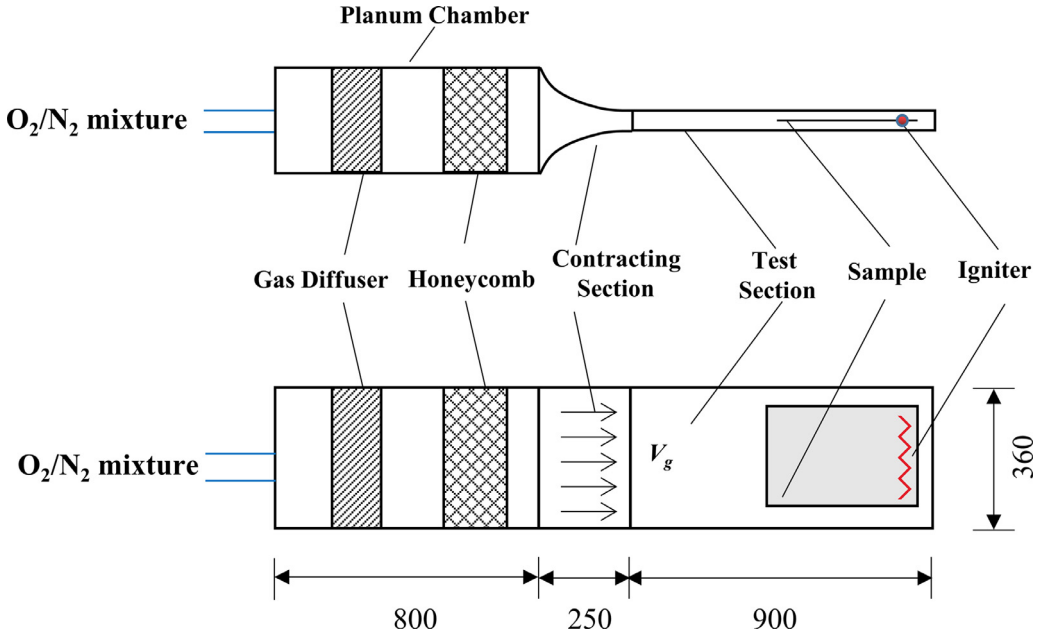

Fig. 4. Schematic of the experimental system. Top: side view; bottom: top view. Unit: (mm).

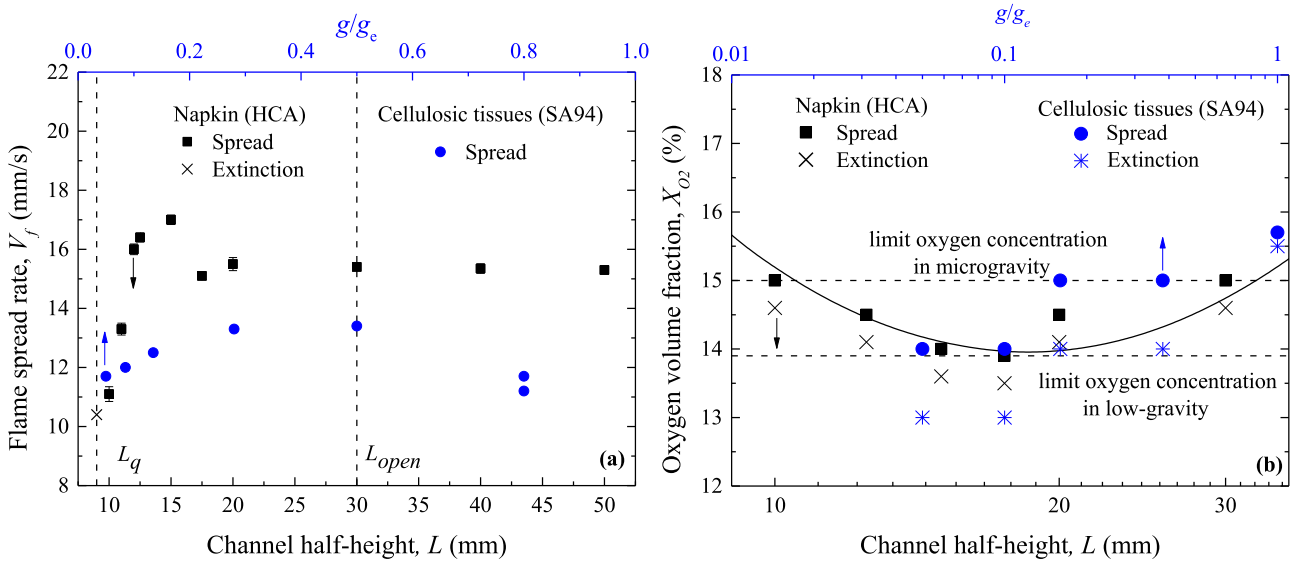

Fig. 5. (a) The flame spread rates (b) the flammability limit boundary as a function of L and g/g_e. For flame spread (extinctions), the square (cross) and circle (asterisk) points denote the results from the HCA and SA94, respectively.

4. Results

4.1. Buoyancy-controlled flame spread

Figure 5(a) presents the experimental results for the flame spread rates in purely buoyant flow as a function of L from the HCA and g/g_e from SA94 with the ambient oxygen concentration fixed at X_{O2} = 21%. Two critical channel heights are observed in Fig. 5(a). As V_f is almost constant at L > 30 mm, the buoyancy is no longer suppressed by the HCA geometry. Accordingly, such upper critical channel height is defined as L_{open}. Corresponding to the "quenching limit", the other critical channel height L_q, below which the flame extinguishes, is also observed. For the napkin paper, L_q is 9 mm. The existence of L_q is also validated in other studies, e.g., Wichman et al. [24] reported L_q = 10 mm for the ashless filters, with a slight difference compared to L_q = 9 mm in the current study. In addition to two critical channel heights, the non-monotonic tendency between V_f and g/g_e reported in SA94 and between V_f and L for the HCA are observed.

Figure 5(b) shows the flammability map of the flame spread over the napkin paper within the HCA, as a function of the ambient oxygen concentration X_{O2} versus L and g/g_e. The accuracy of limit oxygen concentration in parabolic flight is only 1%, mainly due to the limitation of experimental conditions. However, the oxygen concentration in normal gravity is easier to adjust and a more concise flammability map can be easily obtained. Therefore, it seems that the flammability map in HCA is more sensitive to the change of oxygen concentration. In general, the "U" shape flamma-

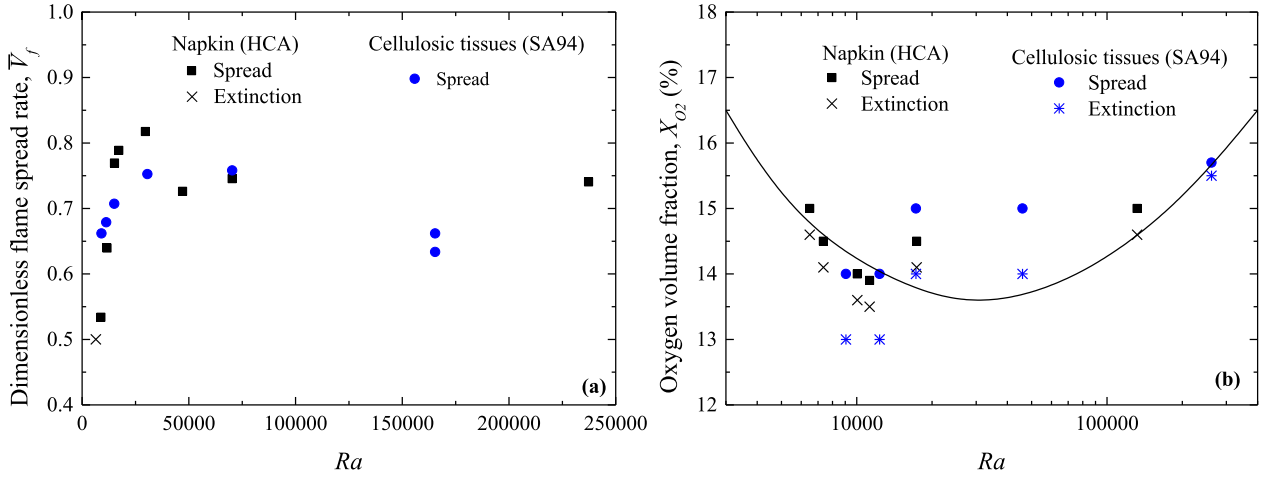

Fig. 6. The (a) dimensional flame spread rate in Fig. 5(a) and (b) flammability boundary in Fig. 5(b) as a function of *Ra*.

bility boundary reported in SA94, whose original form is the variations between X_{O2} versus g/g_e, is also similar to the variations between X_{O2} versus L obtained from the HCA experiments. Especially, the lowest oxygen concentration $X_{O2,lim}$ on flammability boundary for the HCA is about 14% at $L = 17.5$ mm, which is almost same as $X_{O2,lim} = 13.5\%$ at $g/g_e = 0.05 \sim 0.1$ for thin cellulosic tissues reported from SA94 [28]. Such $X_{O2,lim} = 14\%$ does not exist in open-space environment [28] whose $X_{O2,lim}$ is 15.6% and in NCA [44] and microgravity environment [8,10] whose $X_{O2,lim}$ is 15%. The well-correlated flammability boundary as well as $X_{O2,lim} = 14\%$ implies that the HCA can reproduce the flammability map, which is the other global characteristic of the opposed flame spread over solids.

To unify the role of L and g/g_e in representing buoyancy, *Ra* correlations as proposed in Section 2, are applied to the flame spread rates and the flammability boundary in previous Fig. 5, in which the flame spread rates for both fuels are made by dividing experimental data with the theoretical flame spread rate from DeRis [29]:

$$\overline{V}_f = \rho_{area} V_f \frac{c_s(T_v - T_\infty)}{\sqrt{2}\lambda_g(T_f - T_v)} \tag{13}$$

where T_v, T_f, and T_∞ represent the temperature of the vaporization, the flame, and the ambient atmosphere, ρ_{area} represents the area density of the fuel, c_s is the specific heat of the solid phase, λ_g is the thermal conductivity of the gas phase. The values of parameters for calculations are listed in Table 1. Overall, good correlations are obtained as shown in Fig. 6. For the flame spread rates (Fig. 6(a)), noticeably, the critical *Ra* where extinction occurs is at the order of 10^3 as same as the classic critical $Ra = 1700$, where the hydro-thermal dynamics are completely suppressed and give way to thermal conduction [14,47]. Based on similar magnitude order of *Ra*, near the quenching limit, the buoyancy induced by flame spread is also completely suppressed by the HCA. The suppressed buoyancy further leads to insufficient oxygen transportation to sustain the flame spread, which is why the quenching limit occurs in the HCA. With the gradual increase of buoyancy in terms of increased *Ra*, the oxygen transportation is also enhanced, so that V_f increases with *Ra* and therefore L and g/g_e. Once *Ra* further increases to the degree where L_c=L_{open}, the flame is no longer suppressed by the geometry as suggested before, therefore the buoyancy in the HCA ceases increasing further and becoming relatively stable. In contrast, for SA94 where the buoyancy could further increase via increased g/g_e, the flame spread is subject to the effects of chemical kinetics. The stable buoyancy in the HCA and increasing buoyancy for the SA 94 is the reason why there exist certain differences when $Ra > 15{,}000$ in Fig. 6(a) and (b). Based on the similar dependences of buoyancy on *Ra*, the flammability boundary, though slightly different from Fig. 5(b), is well correlated with *Ra*.

The successful *Ra* correlations shown above convincingly indicate that the HCA can create the reduced buoyancy environment, at least for the opposed flame spread over thermally thin fuels. This is reasonable, as *Ra* unifies the influences of L and g in their contributions to buoyancy. As long as the governing *Ra* is at the same level, the same thermally convective flow pattern would always occur, regardless of whether the thermal convection is induced by the reduced geometrical size or the reduced gravitational environment.

It should be noted that the flame spread rates in HCA are not completely the same as that in HCA, mainly due to the following reasons. Firstly, the buoyant flow direction is different in two sets of experiments. The flame spread horizontally in HCA, but downwardly in parabolic flight. The different buoyant flow directions will result in some differences in the heat transfer from the flame to the solid fuel. Secondly, due to the existence of the top wall, it will cool the flame in HCA. However, the chamber in SA94 is much larger, which will not cool the flame. HCA can give a general trend of flame spread in reduced gravity and it is necessary to conduct more reduced gravity experiments to obtain more accurate data. In general, the agreeable correlations of the overall non-monotonic variations between V_f and V_b, strongly suggest that the HCA can reproduce the global characteristics of the opposed flame spread rate at the different gravitational environments, at least to a satisfactory degree.

4.2. Flame spread under combined effects of buoyant and forced flow

Figure 7(a) and (b) show the flame spread rates as a function of the opposed flow velocity V_g and the Reynolds number *Re* within the HCA of different heights. *Re* is defined as:

$$Re = \frac{V_g L}{\nu} \tag{14}$$

following the tradition from the hydro/thermal dynamics community. The $V_f \sim V_g$ results of thermally-thin cellulosic fuels whose area density is 10 g/m^2 obtained in Mg experiments [10] are also included for comparison. The flame spread rates are corrected by the area density. The data in SA94 are excluded as it only involves the flame spread in purely buoyant flow.

When $L \leq 8$ mm (solid points in Fig. 7) the non-monotonic variations between V_f and V_g are obtained, with the flame spread rates in HCA varying around those from the microgravity experi-

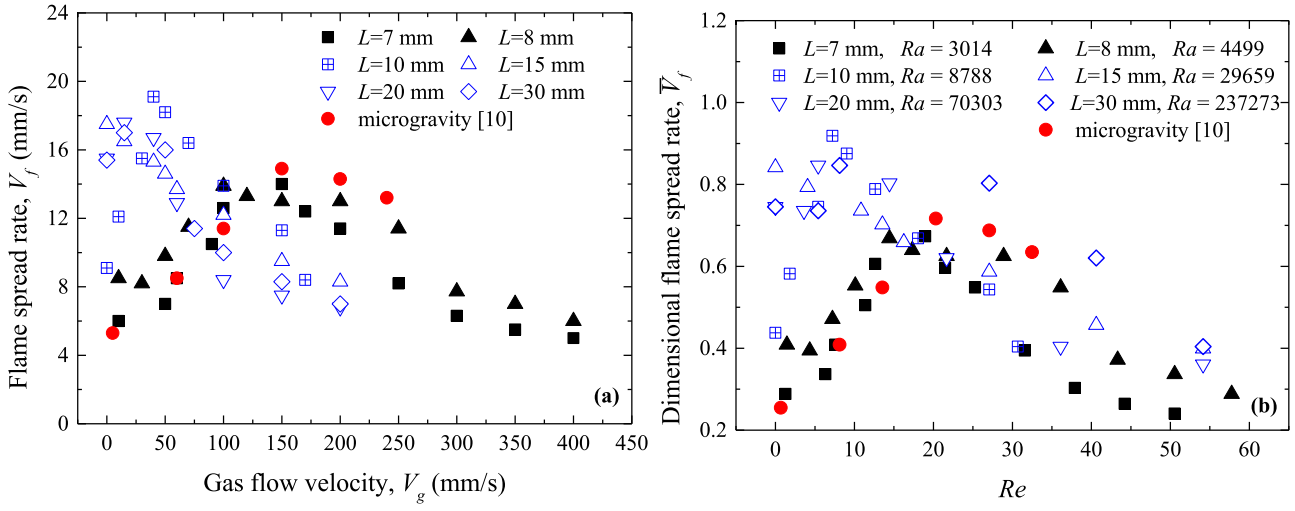

Fig. 7. Flame spread rate as a function of (a) V_g and (b) Reynolds number in the HCA with different heights. The microgravity data from [10] are also included for comparison. The solid points indicate the $V_f \sim V_g$ variations that could correlate with the trend of microgravity data, while the void points indicate the $V_f \sim V_g$ variations that deviate from the trend of microgravity data.

ments [10]. The early ascending stage where V_f increases with V_g as V_g < 150 mm/s, is mainly attributed to the enhanced mixed convection as forced convection is introduced and augmented. Yet, the buoyancy is still subdued, e.g., at L = 8 mm Ra = 4499 is still at the same order of 10^3 as those in the NCA. At such suppressed buoyancy level, the wall heat loss, as proposed by [42], are also important in the overall energy balance. As V_g further exceeds 150 mm/s, the forced convection dominates so that the residual time of the flame is less than the necessary chemical reaction time [4], as a result, V_f decreases with V_g.

When L > 8 mm, the $V_f \sim V_g$ variations deviate from those with $L \leq$ 8 mm and the Mg experiments [10]. Especially, at L = 10 mm, though the non-monotonic tendency remains, the maximum flame spread rate $V_{f,\max}$ occurs at V_g = 40 mm/s, with its magnitudes about twice of those at $L \leq$ 8 mm and larger than $V_{f,\max}$ at quiescent HCA in Fig. 5, at forced convection environment at Mg [8,10], NCA [44] and reported in SA94 [28]. In other words, $V_{f,\max}$ with L = 10 mm at V_g = 40 mm/s perhaps is the maximum flame spread rate among all reduced buoyancy environments, strongly indicating the most promotive environment for opposed flame spread yet the most hazardous environment for fire safety.

At L = 15 and 20 mm, the ascending variations are further weakened, indicating that the overall $V_f \sim V_g$ variations are similar to those from Fernandez-Pello et al. [4] at normal gravity conditions. Likewise, a similar tendency repeat when we further extend L beyond 20 mm, therefore L_{open} = 20 mm is suggested at a mixed convection environment, smaller than L_{open} = 30 mm in purely buoyant flow (Fig. 5) due to apparent enhanced mixed convection.

The deviations of $V_f \sim V_g$ behaviors at L = 10–20 mm and ostensible increasing magnitudes V_f are attributed to unique flame structures determined by the hydro and thermodynamics. Fig. 8 shows the side view images of typical flame spread at L = 5–30 mm and fixed V_g = 5 mm/s, with corresponding Ra and Re denoted. At L = 5 mm (Fig. 8(a)), the flame on the top of the sample holder is so weak that the flame front appears partly symmetric, which is similar to previous studies under buoyancy-suppressed environment (e.g. NCA [44] and Mg condition [8,10]) and therefore indicates the buoyancy within is severely suppressed. As L increases to 10~15 mm (Fig. 8(b)~(c)), the top flame gradually grows strong than its downside counterpart, with its tail curling towards the flame spread direction. Particularly, at L = 20 mm (Fig. 8(d)), the "rolling flame" as marked by the red circle is developed similar to the appearances of concurrent flame spread. Because of such rolling flame structures, more unburnt fuels are exposed to the extended flame region and are further pyrolyzed to provide more vaporized fuel to sustain such a robust flame. Hence, the presence of such rolling flame structure at partly suppressed buoyancy environment is the reason why V_f at L = 10–20 mm is significantly larger in previous Fig. 7. Meanwhile, we also observed that the rolling flames structure is more sensitive to V_g at L = 10 mm, that is also why also in Fig. 7, non-monotonic $V_f \sim V_g$ variation seems more obvious than those below L = 10 mm.

From the view of hydro-thermal dynamics, such rolling flame could also be considered as a single transverse vortex structure, which is similar to the transverse roll structures of the RBP flow. Analogously, Ra = 8788 ~ 29,659 at L = 10 ~ 15 mm is also in the same range where the transverse roll structures appear in the RBP flows [48,49]. Hence, we suggest the rolling flame is the direct consequence of the partly suppressed buoyancy. Of course, in the RBP flows the heat source usually refers to the entire or majority of the fixed bottom boundary, therefore a series of transverse vortex rolls are created. In the current flame spread in the HCA, the heat source is limited to the flame and pyrolyzed fuel region, so that only a single vortex structure, that is, the rolling flame is observed. The dynamical heat source region is also the key difference of the flame spread from the RBP flow, nevertheless, the governing role of Ra and Re should be the same, which will be further confirmed in section 4.3.

At last when L = 20~30 mm, the upright flame agrees with what we usually observed on the ground. It is also found that the flame is no longer suppressed by the channel wall at L = 30 mm, thus the characteristic length scale and corresponding Ra become relatively stable at the order of 10^6. This is also why the ascending stage of $V_f \sim V_g$ no longer exists in the previous Fig. 7.

A unique extinction boundary for the HCA, as shown in Fig. 9(a), consists of L and V_g at fixed ambient oxygen concentration X_{O2} = 21%. Figure 9(b) transfers $L \sim V_g$ into dimensionless $Ra \sim Re$ form. As the opposed flow velocity V_g is introduced, the quenching height L_q, below which the flame extinguishes, also decreases with increased V_g. The maximum quenching height is 9 mm in Fig. 9(a) corresponds to that in the buoyant flow environment as shown in Fig. 5, therefore defined as $L_{q,\max}$. As V_g increases, the quenching height L_q decreases along the flammability boundary until 2.5 mm, below which the flame extinguishes

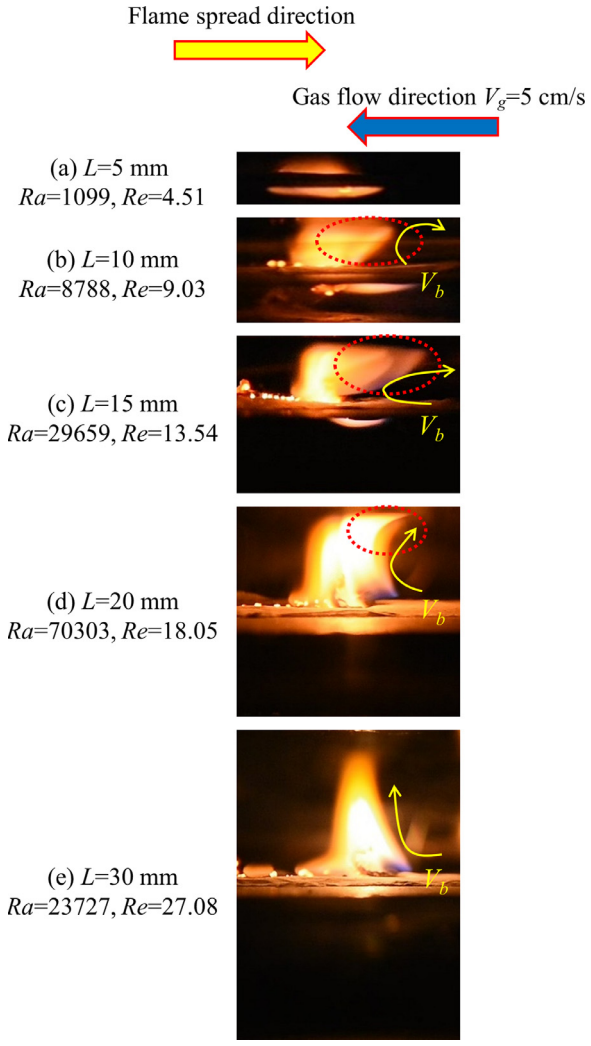

Fig. 8. Side view flame images in HCA at various channel heights.

regardless of V_g. Such lowest quenching height denoted as $L_{q,\min}$ in Fig. 9(a) and (b), agrees with the one reported from previous studies on the NCA [24]. As a result, the overall flammability area is bounded between $L_{q,\max}$ and $L_{q,\min}$. The corresponding critical $Ra_{q,\max}$ and $Ra_{q,\min}$ for $L_{q,\max}$ and $L_{q,\min}$, as shown in Fig. 9(b), is 6406 and 562.

When L is close to the L_g, the space for the gaseous reaction is not enough and the cooling effect of the wall surface is gradually significant, which will lead to the quenching limit. When the opposed flow is introduced into the channel, the characteristic gas-phase length $L_g \sim \alpha_g / V_g$ will decrease with the increased gas flow velocity, and the flame can be survived at L_q due to sufficient oxygen supply. Besides, the previous study shows that the cooling effect of the wall is decreased with the velocity [42]. These factors together promote flame spread. The increased flow velocity will decrease gas-phase length so that the flame spread is accelerated. However, when V_g is sufficiently large, the residence time of the fuel vapor/oxidizer mixture in the flow may approach or even be lower than the chemical reaction time, and the flame will be blown off. Thus, there is a limit channel height $L_{q,\min}$ that the flame cannot spread at any forced flow velocity.

4.3. Flame spread patterns

Previous experimental studies showed that when the flow velocity is near the quenching limit [13] and the sample width is wider than the oxygen diffusion length [18] in buoyancy-suppressed conditions, the uniform flame will break into flamelets. To investigate the effects of buoyancy on the flame spread pattern, the width of the sample will be extended significantly from 35 mm to 200 mm in this subsection.

In general, as L and V_g increase and depart from the quenching limit, the appearances of the flame spread in the HCA always transit from the feeble "fingering" instability near the quenching limit to the continuous and robust flame edge. Distinctively different flame spread patterns 1 ~ 4, as shown in Fig. 10, exist in the transitions. The flame spread pattern 1 is the well-studied "flamelets" or "finger" instability near the quenching limit with NCA, as shown in Fig. 10(a). The track of split flamelets spread form the "finger" shape, which is the result of thermally diffusive transportation of the oxidizer [13,14,18].

The flame spread pattern 2, which occurs once the oxygen transportation via buoyancy is enhanced with increased L, involved distinctively different mechanisms as shown in Fig. 10(b). Unlike pattern 1 where a single flamelet usually occurs somewhere away from the edge of the sample holder, in pattern 2 the flame spread only occurs near the edge of the sample holder. The only existence of the flame near the edge indicates certain flow structures are limited near the edge. Though not shown here, once the buoyancy

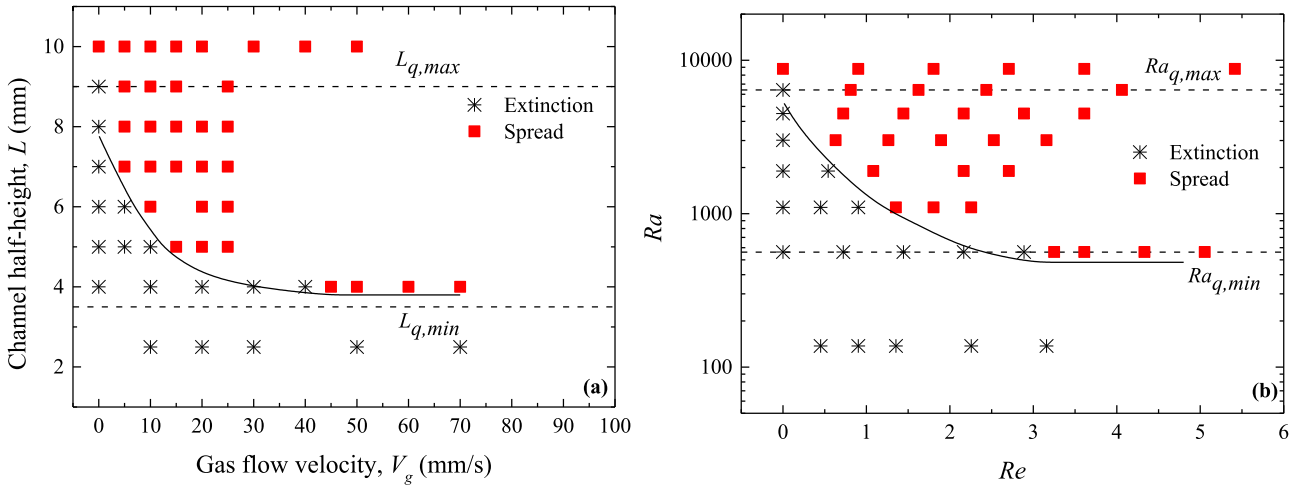

Fig. 9. The flammability boundary as a function of (a) channel height L and flow velocity V_g as well as (b) Ra and Re for the HCA.

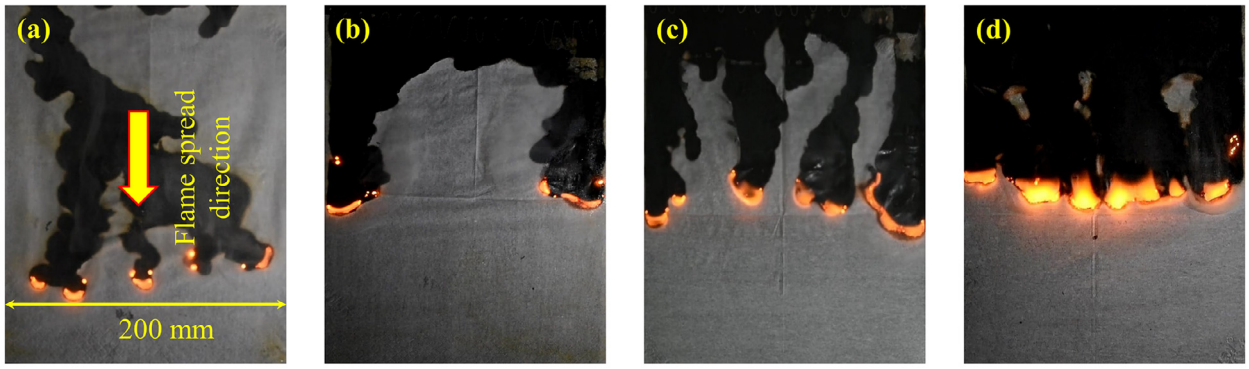

Fig. 10. The typical images and the tracks of flamelets of flame spread patterns 1 ~ 4.

within the HCA is further increased with L, the two edge flamelets extended their width towards the central marginal regions, eventually joining together to become the continuous flame edge.

The flame spread pattern 3, whose typical image is shown in Fig. 10(c), involves similar appearances of flamelets as pattern 1. Nevertheless, the flamelets in pattern 3 spread in parallel with each other and barely bifurcate like those in pattern 1. The overall flame spread in pattern 3 behaves more vigorously than patterns 1 and 2.

The flame spread pattern 4, as shown in Fig. 10(d), appears to be a corrugated and bounded group of flamelets, as indicated by almost burnt solid fuel after the flamelets passed by. Nevertheless, different from the continuous flame edge, each flamelet in pattern 4 is still identifiable so that the overall flame fluctuates during its spreading.

Similar to the flame spread rate V_f signifying the intensity of the stable flame spread in §4.1, a global property is needed to indicate the quantitative influences of $Ra \sim Re$ on the flame spread pattern, in addition to the phenomenal identifications based on the flame spread appearances only. Zik [14] employed the width of "fingers" and their in-between gaps to describe the influences of the lateral oxygen transportation and the geometry of the "fingering" instability and successfully correlated them with the Péclet number Pe. Nevertheless, unlike the "fingering" instability near the quenching limit, the width of flamelets, as well as the gaps in-between, are not stable for the flame spread pattern 2 ~ 4. The average mass loss rate $\overline{\dot{m}}$ could serve as a statistically global property to indicate the overall intensity of the flame spread, defined as:

$$\overline{\dot{m}} = \frac{\rho_{area}(A_2 - A_1)}{\Delta t} \tag{15}$$

where A_1 and A_2 respectively represent the area of the burned sample at the initial and final time, Δt represents burning time. With Eq. (15), the map of $\overline{\dot{m}}$ corresponding to the patterns 1 ~ 4 could be established. The average mass loss rates have significant differences under different flame spread patterns, as shown in Fig. 11.

The agreeable correlations between $\overline{\dot{m}}$ and Re are shown in Fig. 11(a), in which $\overline{\dot{m}}$ for patterns 1 ~ 4 are unified. As:

$$Pe = Re \cdot Sc \tag{16}$$

where $Sc = \nu/D$ represents the Schmidt number, Re is directly associated with Pe, which was employed by Zik [14] as the governing parameter for the "fingering" instability. Once Sc is stable, Re is proportional to Pe. As a result, good correlations between $\overline{\dot{m}}$ and Pe is also expected. As $\overline{\dot{m}}$ indirectly indicates the ratio between the flame and the sample width based on its definition in Eq.(15), the correlations between $\overline{\dot{m}}$ and Re in Fig. 11 agree with the successful correlations between the width of the "finger" and Pe reported by Zik [14]. The good correlations observed in Fig. 11 also suggest that the advective transportation of the oxidizer in terms of Re or Pe is still the dominant mechanism that determines the intensity of the flame spread.

Based on the correlations via Re, $\overline{\dot{m}}$ asymptotically increases with increased Re. Yet, such ascending variations cease at $L = 15$ mm ($Ra = 29{,}659$), in which almost constant $\overline{\dot{m}}$ with absolutely dominant magnitudes over those at $L < 15$ mm is observed, indicating that once L (Ra) reach critical value, the advection of the oxidizer in terms of Re have little influences on $\overline{\dot{m}}$. Coincidentally, such critical value of $L = 15$ mm ($Ra = 29{,}659$) also corresponds to the channel height where the maximum stable flame spread rate occurs as reported in §4.1, indicating the most favorable reduced buoyancy environment for the flame spread may be responsible for the transitional behavior of $\overline{\dot{m}}$.

The variations of $\overline{\dot{m}}$ as a function of Ra are shown in Fig. 11(b). Several branches are bifurcated from the concentrated regions near the critical $Ra = 29{,}659$ where Re is independent of $\overline{\dot{m}}$ and split further with increasing gaps as Ra decreases. Because all flame spread patterns are unified via the correlations of Re in Fig. 11(a) yet are distinguished via the correlations of Ra in Fig. 11(b), the bifurcations as Ra decreases from the critical $Ra = 29{,}659$ strongly suggest that the role of reduced buoyancy is to invoke different flame spread patterns, which is similar to the role of Ra in determining the instabilities of the RBP flow.

Together with Ra and Re, the map of flame spread pattern 1~4 (directly denoted by the symbols from "1" ~ "4") and the contour of $\overline{\dot{m}}$ are plotted in Fig. 12. The effective regions of the pattern 1 ~ 4 are bounded by the extinction boundary indicating the quenching limit and the transitional boundary indicating the continuous flame edge. As individual regions of the patterns 1 ~ 4 and the contour of $\overline{\dot{m}}$ are well distinguished by $Re \sim Ra$, once again $Re \sim Ra$ is proved to be the governing parameters for the flame spread within the HCA, and therefore the overall flame dynamics are mainly dominated by the hydro and thermal dynamics. Nevertheless, as the area of the flame is dynamically coupled with the oxygen transportation, the flame spread in the HCA includes more instability modes, namely, the patterns 1 ~ 4, compared to the RBP flow which only involves a stable heated area and thereby two types of instabilities.

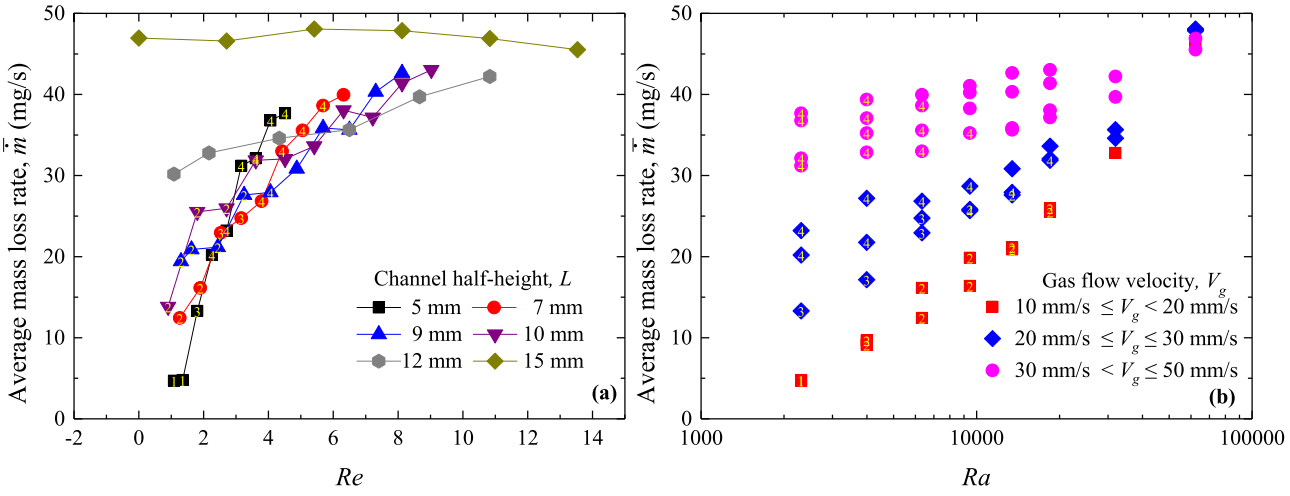

Fig. 11. The time average mass loss rate $\overline{\dot{m}}$ as a function of (a) *Re* and (b) *Ra*. The symbols "1" to "4" represent the flame spread pattern 1 ~ 4.

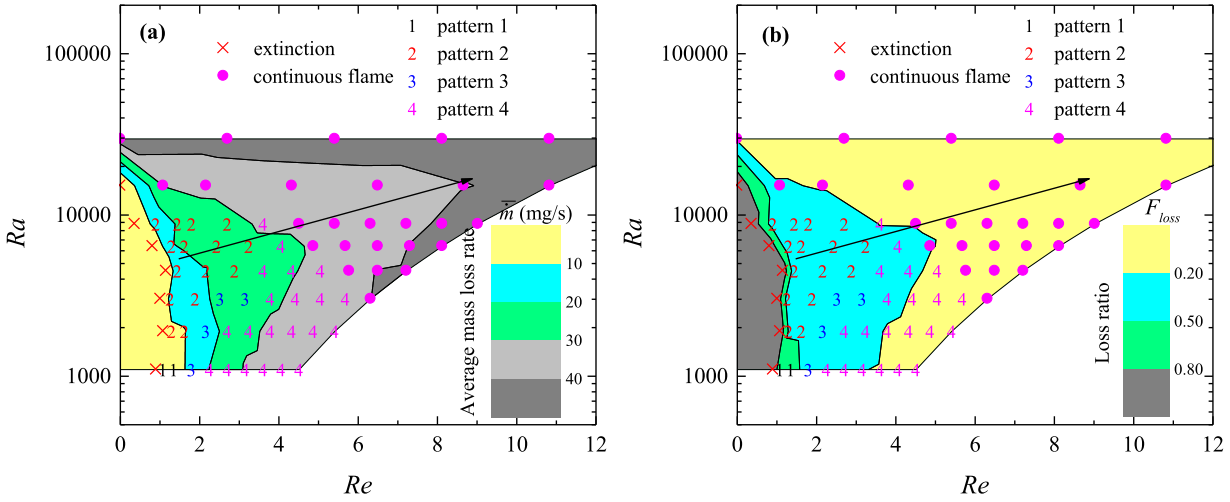

Fig. 12. The contour of $\overline{\dot{m}}$ and F_{loss} as a function of *Re* and *Ra*. The magnitudes of $\overline{\dot{m}}$ and F_{loss} are indicated in different colors, as indicated by the palette.

Furthermore, radiative heat loss plays a significant role in flame spread issues compared to the RBP flow, especially when the flame spreads near the quenching limit. Near the flame leading edge, the flame conduction is balanced with the radiative heat loss from the fuel surface to the ambient and the sensible energy to preheat the fuel. The energy balance at the surface of fuel can be expressed as:

$$\dot{q}_{cond,f} = c_s \overline{\dot{m}}(T_v - T_\infty) + \varepsilon\sigma(T_v^4 - T_\infty^4)L_g w \tag{17}$$

where w is the sample width, $w = 200$ mm; L_g is assumed to equal to pyrolysis length, $L_g = 2$ mm. The heat loss ratio is defined as [13]:

$$F_{loss} = \frac{\varepsilon\sigma(T_v^4 - T_\infty^4)}{c_s \overline{\dot{m}}(T_v - T_\infty)/(L_g w) + \varepsilon\sigma(T_v^4 - T_\infty^4)} \tag{18}$$

The F_{loss} as a function of *Re* and *Ra* is plotted in Fig. 12(b). It can be seen that the heat loss ratio is increased with the decrease of *Re* at the given *Ra*. Near the extinction limit, the heat loss ratio is above 70%, which agrees with microgravity experiments for the ashless filter [13]. Note that even when *Ra* increases to the order of 10^4 where the buoyancy is reduced rather than suppressed, near extinctions F_{loss} still reach above 70%, indicating the radiation heat loss remains the crucial contributor to the quenching limit. The reduced role of radiation heat loss in a buoyancy-reduced environment could also be the reason why the limit oxygen concentration in Fig. 6 is lower than those at buoyancy-suppressed environments such as Mg condition and NCA. Nonetheless, because of the enhanced buoyancy, the regions of F_{loss}=0.5–0.8 (green area) become thinner and occur at smaller *Re*=0~2 at *Ra*~10^4. In fact, as the majority of buoyancy-reduced environments belong to the cyan or yellow area where F_{loss}=0–0.5, the role of the radiation heat loss is remarkably compromised. This could be considered as an important feature of the flame spread in the buoyancy-reduced environment. Moreover, different flame spread patterns further complicate the role of radiation heat loss. For instance, we find that in general the pattern 2 involves less F_{loss} than pattern 3 when *Re* is the same, which also agrees with Fig. 12(a) where pattern 2 involves larger $\overline{\dot{m}}$ than pattern 3. Therefore, the specific flame spread patterns must be considered when one analyzes the energy balance for the buoyancy-reduced environment.

5. Conclusion

As the extension of the NCA in terms of channel height *L*, the HCA is employed to investigate the opposed flame spread over the solid fuel under suppressed buoyant flow conditions. The global characteristics including flame spread rates and flammability boundary along with the flame spread patterns were examined, within the HCA with channel height *L* and opposed flow velocity V_g, namely, different *Ra* and *Re*.

The scaling analysis and correlations exhibit that the characteristic buoyant flow velocity V_b and associated Ra derived from the parabolic flight experimental results reported in SA94 could be well correlated with those from the current HCA experiments, indicating the reduced buoyancy environment induced by the partial gravity and the HCA are governed by the same mechanisms. Based on the good correlations of V_b and Ra, excellent agreement of flame spread rates and flammability between SA94 and the current study are also obtained. Also, a special flammability map built by L and V_g, alternatively, Ra versus Re, defines the effective regions where the buoyancy induced by the flame spread is suppressed. The extinction boundary corresponding to the quenching limit is also significantly extended from the previous studies based on the NCA and Mg experiments. The special "rolling flame" structures, which are similar to the transverse vortex rolls in the RBP flow, are observed when Ra is at the order $10^3 \sim 10^4$. Such unique flame structures lead to the deviations of $V_f \sim V_g$ behaviors in the buoyancy-reduced environment compared to those at buoyancy-suppressed one such as NCA and Mg condition.

Once the sample width is extended, four distinctively unstable flame spread patterns are found within the transitional regions from the thermal-diffusive "fingering" instability to the continuous flame edge. The unique features of these four patterns as well as their transition to the continuous flame edge are analyzed. Further examinations of $\overline{\dot{m}}$ suggest that Re is the main governing parameter of the flame regions in terms of $\overline{\dot{m}}$, while Ra is the main governing parameter that determines the transitions among the flame spread patterns. Nevertheless, the influences of Ra and Re only exist in the effective regions where $Ra < 29{,}659$. Near the quenching limit, the radiation heat loss remains important in energy balance for the buoyancy-reduced environment when Re is small. Nevertheless, the overall contribution of the radiation heat loss in the buoyancy-reduced environment is significantly reduced. Furthermore, the different flame spread patterns also involve different F_{loss}.

Declaration of Competing Interest

The authors declare that they have no known competing financial interests or personal relationships that could have appeared to influence the work reported in this paper.

Acknowledgment

This work is supported by the National Key R&D Program of China (Grant No. 2021YFA0716203), the National Natural Science Foundation of China (Grant No. U1738117), and the early career development program of China East Jiaotong University (Grant No. 10032003419068).

References

[1] S.R. Tieszen, On the fluid mechanics of fires, Annu. Rev. Fluid Mech. 33 (2001) 67–92, doi:10.1146/annurev.fluid.33.1.67.
[2] A.C. Fernandez-Pello, Flame spread in a forward forced flow, Combust. Flame. 36 (1979) 63–78, doi:10.1016/0010-2180(79)90046-4.
[3] A.C. Fernandez-Pello, S.R. Ray, I. Glassman, Downward flame spread in an opposed forced flow, Combust. Sci. Technol. 19 (1978) 19–30, doi:10.1080/00102207808946860.
[4] A.C. Fernandez-Pello, S.R. Ray, I. Glassman, Flame spread in an opposed forced flow: the effect of ambient oxygen concentration, Symp. Combust. 18 (1981) 579–589, doi:10.1016/S0082-0784(81)80063-X.
[5] R.A. Altenkirch, R. Eichhorn, P.C. Shang, Buoyancy effects on flames spreading down thermally thin fuels, Combust. Flame. 37 (1980) 71–83, doi:10.1016/0010-2180(80)90072-3.
[6] L. Zhou, A.C. Fernandez-Pello, Turbulent, concurrent, ceiling flame spread: the effect of buoyancy, Combust. Flame. 92 (1993) 45–59, doi:10.1016/0010-2180(93)90197-B.
[7] E. Fernández-Tarrazo, A. Liñán, Flame spread over solid fuels in opposite natural convection, Proc. Combust. Inst. 29 (2002) 219–225, doi:10.1016/S1540-7489(02)80030-X.
[8] S.L. Olson, P.V. Ferkul, J.S. T'ien, Near-limit flame spread over a thin solid fuel in microgravity, Symp. Combust. 22 (1989) 1213–1222, doi:10.1016/S0082-0784(89)80132-8.
[9] F. Zhu, Z. Lu, S. Wang, Y. Yin, Microgravity diffusion flame spread over a thick solid in step-changed low-velocity opposed flows, Combust. Flame. 205 (2019) 55–67, doi:10.1016/j.combustflame.2019.03.040.
[10] S.L. Olson, Mechanisms of microgravity flame spread over a thin solid fuel: oxygen and opposed flow effects, Combust. Sci. Technol. 76 (1991) 233–249, doi:10.1080/00102209108951711.
[11] X. Huang, J. Gao, A review of near-limit opposed fire spread, Fire Saf. J. 120 (2021) 103141, doi:10.1016/j.firesaf.2020.103141.
[12] A.V. Ivanov, Y.V. Balashov, T.V. Andreeva, A.S. Melikhov, Experimental Flammability Verification in Space of Material, 1999.
[13] S.L. Olson, F.J. Miller, S. Jahangirian, I.S. Wichman, Flame spread over thin fuels in actual and simulated microgravity conditions, Combust. Flame. 156 (2009) 1214–1226, doi:10.1016/j.combustflame.2009.01.015.
[14] O. Zik, Z. Olami, E. Moses, Fingering instability in combustion, Phys. Rev. Lett. 81 (1998) 3868–3871, doi:10.1103/PhysRevLett.81.3868.
[15] O. Zik, E. Moses, Fingering instability in combustion: an extended view, Phys. Rev. E. 60 (1999) 518–531, doi:10.1103/PhysRevE.60.518.
[16] O. Zik, E. Moses, Fingering instability in solid fuel combustion: the characteristic scales of the developed state, Symp. Combust. 27 (1998) 2815–2820, doi:10.1016/S0082-0784(98)80139-2.
[17] S.L. Olson, H.R. Baum, T. Kashiwagi, Finger-like smoldering over thin cellulosic sheets in microgravity, Symp. Combust. 27 (1998) 2525–2533, doi:10.1016/S0082-0784(98)80104-5.
[18] X. Zhang, Y. Yu, Experimental studies on the three-dimensional effects of opposed-flow flame spread over thin solid materials, Combust. Flame. 158 (2011) 1193–1200, doi:10.1016/j.combustflame.2010.10.004.
[19] S. Wang, S. Wang, K. Zhu, Y. Xiao, Z. Lu, Near quenching limit instabilities of concurrent flame spread over thin solid fuel, Combust. Sci. Technol. 188 (2016) 451–471, doi:10.1080/00102202.2015.1125346.
[20] F. Zhu, S. Wang, Z. Lu, A comparative study of near-limit flame spread over a thick solid in space- and ground-based experiments, Microgravity Sci. Technol. 30 (2018) 943–949, doi:10.1007/s12217-018-9655-0.
[21] T. Matsuoka, S. Murakami, T. Yamazaki, Y. Nakamura, Symmetric and nonsymmetric flame spread between parallel plates of thick combustible solid, Combust. Sci. Technol. (2018) 1–19 00, doi:10.1080/00102202.2018.1534838.
[22] K. Kuwana, K. Suzuki, Y. Tada, G. Kushida, Effective Lewis number of smoldering spread over a thin solid in a narrow channel, Proc. Combust. Inst. 36 (2017) 3203–3210, doi:10.1016/j.proci.2016.06.159.
[23] K. Funashima, A. Masuyama, K. Kuwana, G. Kushida, Opposed-flow flame spread in a narrow channel: prediction of flame spread velocity, Proc. Combust. Inst. 37 (2019) 3757–3765, doi:10.1016/j.proci.2018.08.017.
[24] I.S. Wichman, S.L. Olson, F.J. Miller, S.A. Tanaya, Experimental evaluation of flame and flamelet spread over cellulosic materials using the narrow channel apparatus, Fire Mater 37 (2013) 503–519, doi:10.1002/fam.2143.
[25] S. Olson, F. Miller, I. Wichman, Characterizing fingering flamelets using the logistic model, Combust. Theory Model. 10 (2006) 323–347, doi:10.1080/13647830600565446.
[26] S. Hossain, I.S. Wichman, G.W. Sidebotham, S.L. Olson, F.J. Miller, Influence of gap height and flow field on global stoichiometry and heat losses during opposed flow flame spread over thin fuels in simulated microgravity, Combust. Flame. 193 (2018) 133–144, doi:10.1016/j.combustflame.2018.02.023.
[27] B.Z. Dlugogorski, H. Wang, E.M. Kennedy, M.A. Delichatsios, P. Safety, E. Protection, N. Ireland, Testing of gaseous fire suppressants in narrow channel apparatus, Proc. An. Inter. Halon Options Tech. Work. Conf (2002), pp. 1–11.
[28] K.R. Sacksteder, J.S. Tien, Buoyant downward diffusion flame spread and extinction in partial-gravity accelerations, Symp. Combust. 25 (1994) 1685–1692, doi:10.1016/S0082-0784(06)80816-7.
[29] J.N. De Ris, Spread of a laminar diffusion flame, Symp. Combust. 12 (1969) 241–252, doi:10.1016/S0082-0784(69)80407-8.
[30] I.S. Wichman, Flame spread in an opposed flow with a linear velocity gradient, Combust. Flame. 50 (1983) 287–304, doi:10.1016/0010-2180(83)90071-8.
[31] X. Nicolas, Bibliographical review on the Poiseuille–Rayleigh–Bénard flows: the mixed convection flows in horizontal rectangular ducts heated from below, Int. J. Therm. Sci. 41 (2002) 961–1016, doi:10.1016/S1290-0729(02)01374-1.
[32] F. Zhu, Z. Lu, S. Wang, Flame spread and extinction over a thick solid fuel in low-velocity opposed and concurrent flows, Microgravity Sci. Technol. 28 (2016) 87–94, doi:10.1007/s12217-015-9475-4.
[33] S. Hossain, I.S. Wichman, F.J. Miller, S.L. Olson, Opposed flow flame spread over thermally thick solid fuels: buoyant flow suppression, stretch rate theory, and the regressive burning regime, Combust. Flame. 219 (2020) 57–69, doi:10.1016/j.combustflame.2020.05.001.
[34] G.J. Sheard, M.P. King, Horizontal convection: effect of aspect ratio on Rayleigh number scaling and stability, Appl. Math. Model. 35 (2011) 1647–1655, doi:10.1016/j.apm.2010.09.041.
[35] L.K. Honda, P.D. Ronney, Mechanisms of concurrent-flow flame spread over solid fuel beds, Proc. Combust. Inst. 28 (2000) 2793–2801, doi:10.1016/s0082-0784(00)80701-8.
[36] J.G. Quintiere, Fundamentals of Fire Phenomena, John Wiley & Sons, 2006, doi:10.1002/0470091150.
[37] S. Bhattacharjee, R. Ayala, K. Wakai, S. Takahashi, Opposed-flow flame spread in microgravity-theoretical prediction of spread rate and flammability map, Proc. Combust. Inst. 30 (2005) 2279–2286, doi:10.1016/j.proci.2004.08.020.
[38] S. Bhattacharjee, M.D. King, S. Takahashi, T. Nagumo, K. Wakai, Downward

flame spread over poly(methyl)methacrylate, Proc. Combust. Inst. 28 (2000) 2891–2897, doi:10.1016/S0082-0784(00)80713-4.
[39] S. Bhattacharjee, L. Carmignani, Radiation-kinetics interactions: a comparison of opposed-flow flame spread in a low-velocity microgravity and low-pressure downward environments, Proc. Combust. Inst. (2020) 1–9, doi:10.1016/j.proci.2020.05.014.
[40] A.E. Frey, J.S. T'ien, A theory of flame spread over a solid fuel including finite-rate chemical kinetics, Combust. Flame. 36 (1979) 263–289, doi:10.1016/0010-2180(79)90064-6.
[41] T. Matsuoka, K. Nakashima, T. Yamazaki, Y. Nakamura, Geometrical effects of a narrow channel on flame spread in an opposed flow, Combust. Sci. Technol. 190 (2018) 408–423, doi:10.1080/00102202.2017.1394848.
[42] G.W. Sidebotham, S.L. Olson, P. Rachow, F.J. Miller, I.S. Wichman, Effect of gap height on thin fuel opposed flow flame spread in the narrow channel apparatus, 7th US Natl. Combust. Meet. (2011) 1–6, doi:10.13140/2.1.2678.4640.
[43] B. Comas, A. Carmona, T. Pujol, Experimental study of the channel effect on the flame spread over thin solid fuels, Fire Saf. J. 71 (2015) 162–173, doi:10.1016/j.firesaf.2014.12.001.
[44] Y. Xiao, J. Hu, S.F. Wang, J.F. Zhao, A narrow channel experimental study on flammability characteristics of thermally thin fuels under simulated microgravity conditions, J. Astronaut. 31 (2010) 1877–1882, doi:10.3873/j.issn.1000-1328.2010.07.028.
[45] T.L. Bergman, A.S. Lavine, F.P. Incropera, D.P. Dewitt, Fundamentals of Heat and Mass Transfer, 7th Ed., John Wiley & Sons, 2011.
[46] S.L. Olson, T. Kashiwagi, O. Fujita, M. Kikuchi, K. Ito, Experimental observations of spot radiative ignition and subsequent three-dimensional flame spread over thin cellulose fuels, Combust. Flame. 125 (2001) 852–864, doi:10.1016/S0010-2180(00)00249-2.
[47] P.G. Drazin, W.H. Reid, Hydrodynamic Stability, 2nd Ed., Cambridge University Press, 2004.
[48] W.L. Lin, Y.T. Ker, T.F. Lin, Experimental observation and conjugated heat transfer analysis of vortex flow development in mixed convection of air in a horizontal ressctangular duct, Int. J. Heat Mass Transf. 39 (1996) 3667–3683, doi:10.1016/0017-9310(96)00031-2.
[49] C.H. Yu, M.Y. Chang, T.F. Lin, Structures of moving transverse and mixed rolls in mixed convection of air in a horizontal plane channel, Int. J. Heat Mass Transf. 40 (1997) 333–346, doi:10.1016/0017-9310(96)00099-3.